

# Optic Disk and Cup Segmentation Through Fuzzy Broad Learning System for Glaucoma Screening

Riaz Ali, Bin Sheng , Ping Li , *Member, IEEE*, Yan Chen , Huating Li , Po Yang, Younhyun Jung , Jinman Kim , and C. L. Philip Chen , *Fellow, IEEE*

**Abstract**—Glaucoma is an ocular disease that causes permanent blindness if not cured at an early stage. Cup-to-disk ratio (CDR), obtained by dividing the height of optic cup (OC) with the height of optic disk (OD), is a widely adopted metric used for glaucoma screening. Therefore, accurately segmenting OD and OC is crucial for calculating a CDR. Most methods have employed deep learning methods for the segmentation of OD and OC. However, these methods are very time consuming. In this article, we present a new fuzzy broad learning system-based technique for OD and OC segmentation with glaucoma screening. We comprehensively integrated extracting a region of interest from RGB images, data augmentation, extracting red and green channel images, and inputting them to the two separate fuzzy broad learning system-based neural networks for segmenting the OD and OC, respectively, and then calculated CDR. Experiments show that our fuzzy broad learning system-based technique outperforms many state-of-the-art methods.

**Index Terms**—Broad learning system (BLS), fuzzy system, neural networks, ocular disease, optic disk and cup, segmentation.

## I. INTRODUCTION

GLAUCOMA is an ophthalmic disease that causes damage to the optic disk (OD) [also called the optic nerve head (ONH)]. It is the second prime cause of blindness worldwide and can affect everyone from newborn babies to older people [1]. Glaucoma is usually assessed in three ways, which are: measuring the intraocular pressure, conducting a visual field test, and examining ONH [2]. However, ONH assessment is preferred and practiced widely by experts [3]. Cup-to-disk ratio (CDR) is a clinical measurement that is commonly used by ophthalmologists for ONH assessment [3]. CDR is calculated as the ratio of the vertical diameter of optic cup (OC), a yellowish brighter area at the center of OD, to the vertical diameter of OD. Because internal structures of an eye are affected by the increased pressure caused by glaucoma, the size of OC increases with respect to the size of OD; a phenomenon also called cupping [4]. Thence, usually a larger CDR indicates the presence of glaucoma. Fig. 1 shows a significant difference in sizes of OD and OC in a healthy and glaucomatous eye. Traditionally, clinicians calculated CDR by manually segmenting OD and OC. Yet, manual segmentation takes huge time and is prone to the subjective judgment of ophthalmologists. Hence, there is a need for automatic and fast segmentation of OD and OC for large scale and efficient diagnosis of glaucoma.

Several works have been proposed for OD and OC segmentation. Some of them use deep learning, and some employ nondeep learning-based approaches. The nondeep learning-based methods are not much time consuming, but they usually lack in providing as promising results as deep learning approaches do. These methods mainly consist of color and contrast thresholding, region segmentation, and boundary detection techniques [5], [6]. Most of the modern techniques, which rely on the features such as texture, color, and gradient, do not perform well on the low-contrast images and the images having pathologies [3]. The work of [7] detected and segmented the OD from the retinal fundus image by employing a region growing method. However, it requires high-resolution images for providing optimal results. Conversely, deep learning systems

Manuscript received February 22, 2020; accepted June 1, 2020. Date of publication June 5, 2020; date of current version January 4, 2021. This work was supported in part by the National Natural Science Foundation of China under Grant 61872241 and Grant 61572316, in part by the Science and Technology Commission of Shanghai Municipality under Grant 18410750700, Grant 17411952600, and Grant 16DZ0501100, and in part by The Hong Kong Polytechnic University under Grant P0030419 and Grant P0030929. Paper no. TII-20-0910. (Corresponding authors: Bin Sheng, Yan Chen, and Huating Li.)

Riaz Ali and Bin Sheng are with the Department of Computer Science and Engineering, Shanghai Jiao Tong University, Shanghai 200240, China (e-mail: 47956152@qq.com; shengbin@sjtu.edu.cn).

Ping Li is with the Department of Computing, The Hong Kong Polytechnic University, Kowloon, Hong Kong (e-mail: p.li@polyu.edu.hk).

Yan Chen and Huating Li are with the Shanghai Jiao Tong University Affiliated Sixth People's Hospital, Shanghai 200233, China (e-mail: chenyan363@hotmail.com; huating99@sjtu.edu.cn).

Po Yang is with the Department of Computer Science, The University of Sheffield S1 4DP, Sheffield, U.K. (e-mail: Po.Yang@Sheffield.ac.uk).

Younhyun Jung and Jinman Kim are with the Biomedical and Multimedia Information Technology Research Group, School of Information Technologies, The University of Sydney, Sydney, NSW 2006, Australia (e-mail: yjun6175@uni.sydney.edu.au; jinman.kim@sydney.edu.au).

C. L. Philip Chen is with the School of Computer Science and Engineering, South China University of Technology, Guangzhou 510006, China is with the Navigation College, Dalian Maritime University, Dalian 116026, China, and also with the Faculty of Science and Technology, University of Macau, Macau 999078, China (e-mail: Philip.Chen@ieee.org).

Color versions of one or more of the figures in this article are available online at <https://ieeexplore.ieee.org>.

Digital Object Identifier 10.1109/TII.2020.3000204

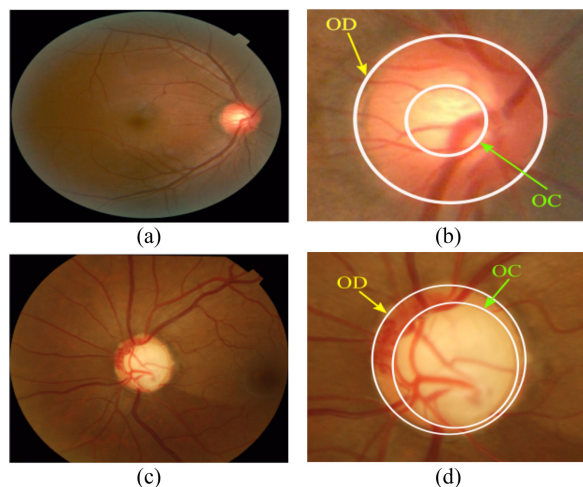


**Fig. 1.** (a) Image of a normal eye. (b) Boundaries of OD and OC in a normal eye. (c) Image of a glaucomatous eye. (d) Boundaries of OD and OC in a glaucoma affected eye.

learn very complex features effectually due to their powerful layer-by-layer feature learning abilities [8]–[10], and therefore, they provide excellent results in image segmentation tasks. Hence, some methods have used deep learning for OD and OC segmentation. The technique in [11] used a fully convolutional neural network (CNN) and transfer learning for OD segmentation. Nonetheless, this method uses a large number of parameters for its model, hence takes a lot of time and graphics processing unit (GPU) memory for training. The technique in [12] also took a long time for predicting the results and was complex and difficult to implement [13]. The works in [3] and other recent deep learning-based methods have performed well on the respective data sets used for their training and testing, but may be unable to provide such accurate results when used practically in hospitals because of the variations like the camera used for capturing the images, quality of images, and the people being diagnosed [14]. The task of OC segmentation is more laborious than OD segmentation because of the existence of blood vessels and the low-contrast boundary. Increasing the neural network size in deep learning helps achieve better segmentation results, but it increases the training time as well. Moreover, some of the methods segment the OD and OC jointly within the same network model, which may not produce splendid segmentation of OC. Thus, a significant challenge in this field is to balance the tradeoff of accuracy and computation cost in utilizing deep learning approaches for OD/OC segmentation for glaucoma detection.

The key reason leading the high computation cost of a deep learning-based system is mainly its complex structure with many layers and a high number of parameters, as shown in Fig. 2(a). Besides, backpropagation is used to fine-tune the network and recalculate the weights. Additionally, the entire network needs to be retrained when new inputs are added to the network. These features make deep learning-based methods consume a lot of time for their training even on the powerful computers having sufficient GPU. In order to solve the problem of balancing the tradeoff of accuracy and computation cost of deep learning technique, one new learning technique called broad learning

system (BLS) with a simpler structure of the flat network [see Fig. 2(b)] was introduced in [15]. It is usually less time consuming than deep learning networks because: 1) its architecture mainly consists of three parts—mapped features, enhancement nodes, and an output layer; 2) its trainable parameters are fewer than deep learning and are easily computed through ridge regression. Also, retraining of the full network is not required in a BLS if the features are to be added later in the network. So, BLS is efficient in training the models in deep structure. Recently, many researchers such as [16] and [17] have employed broad learning in image recognition, image classification, and other computer vision applications, and outperformed the deep learning-based methods significantly in terms of training time.

While the learning accuracy of BLS surpasses the existent deep learning methods and other similar structures [17], [18], one significant problem of BLS is that its generality and stability may be easily degraded due to the existence of outliers and noise in data [19], which may reduce accuracy in ONH analysis because retinal images are sometimes noisy. In order to solve this problem, some authors, such as [20] and [21], have used fuzzy neural networks (FNNs), the learning models which have the merits of both neural networks (by having the virtues of connections and learning behavior) and fuzzy systems (by having IF-THEN fuzzy rules-based humanlike reasoning). According to [22], FNNs have the capability to deal with a problem where the data are imprecise or uncertain, and the task of identifying object boundaries in an image is fuzzy in its nature because it involves imprecision and uncertainty. This property is particularly useful to tiny object detection in real practice medical images or applications such as segmentation of OC because there is no distinct outline of where does the boundary of OC start due to its low-contrast boundary. Recently, Feng *et al.* [16] integrated BLS with fuzzy systems to propose a novel broad learning-based fuzzy learning system called fuzzy BLS (FBLS) which comprises fuzzy subsystems and enhancement nodes. The training process in FBLS is significantly reduced because of its flat network, and the output layer's weights are calculated using pseudoinverse. This system has the combined advantages of both BLS and fuzzy systems.

Therefore, this article targets at finding out a practically effective and efficient glaucoma screening solution by studying the state-of-the-art OD and OC segmentations. Due to the efficiency and performance capability of FBLS, we propose a new method of OD and OC segmentation, which adopts this learning model. We comprehensively integrated extracting a region of interest (ROI) from RGB images, data augmentation, extracting red and green channel images, and inputting them to the two separate FBLS-based neural networks for segmenting the OD and OC, respectively, and then calculated CDR. Experiments show that our FBLS-based technique outperforms state-of-the-art methods, and our approach significantly accelerates the computational time and maintains high accuracy of OD/OC segmentation and glaucoma detection.

The contributions of our work presented in this article are the following.

- 1) A novel broad learning-based FNN is proposed for effective and efficient OD and OC segmentation for glaucoma screening, where the mapped feature nodes of the original

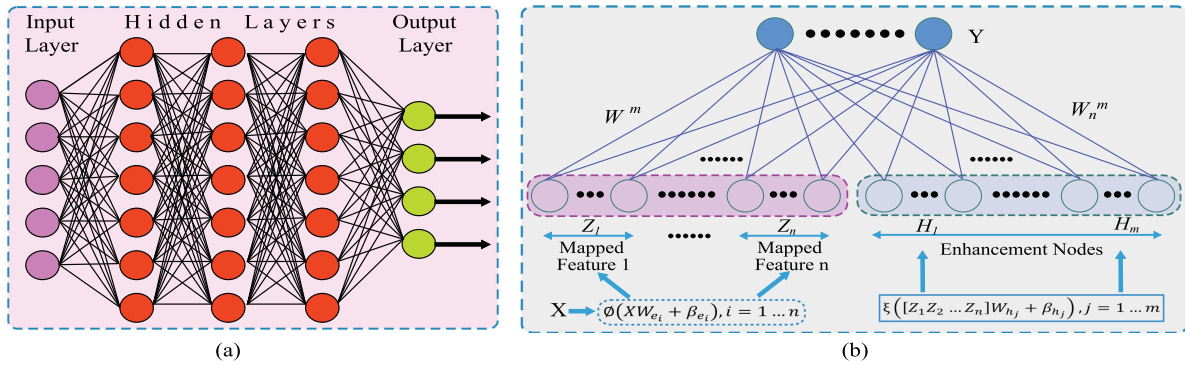


Fig. 2. (a) Structure of a typical deep learning-based neural network. (b) Structure of a typical BLS.

BLS are replaced with Takagi–Sugeno fuzzy subsystems. Each of these fuzzy subsystems processes the input data, hence this method has the advantage of an ensemble structure.

- 2) This approach extracts features more effectively from the input image because it uses the  $k$ -means algorithm to decide the count of fuzzy rules in every fuzzy subsystem and Gaussian membership functions' centers. The application of the  $k$ -means technique produces different centers from the input data for every subsystem, that assures the generation of more distinct features and thus results in the extraction of abundant discriminative information from the input image as compared to BLS.
- 3) An enhanced least square method is designed in the proposed BLS-based fuzzy model to get the final weights with smaller training errors. Also, an  $l_1$ -norm regularization is employed to prohibit the model from overfitting. This makes our approach maintain high accuracy of OD/OC segmentation and glaucoma detection.
- 4) An extensive in-depth and thorough experimental evaluation is carried out to show the robustness and usefulness of our technique. The obtained results exhibit that our method sufficiently outperforms state-of-the-art algorithms in OD and OC segmentation and glaucoma classification. Additionally, for evaluation of glaucoma, we construct a new data set of retinal images called Shanghai Chinese Retinal Images Data Set (SCRID) comprising 566 retinal fundus images.

## II. RELATED WORK

### A. Morphological Operations and Reconstruction

Some of the earlier works use morphological operations and reconstruction for segmenting OD and OC. Nugroho *et al.* [4] introduced morphological reconstruction and convex hull for segmenting OC, while OD is segmented by combining morphological reconstruction and active contour. However, active contour models depend on a proper initialization of OD contour for providing optimal results [14]. In [23], the dilation operation was used to overcome the problem of the misclassifying area around the retina after applying thresholding. They also use opening followed by dilation to remove the irregularity of segmented OD and to give proper disk size. For segmenting

cup, they use a closing operation to remove blood vasculature in the green color channel. The work of [24] involved dilation and erosion operations to eliminate blood vessels in OD, and to smoothen the intensity around OD. Similarly, [25] also used morphological operations for removing retinal vasculature and other pathologies and enhancing OD for getting more accurate segmentation.

### B. $K$ -Means Clustering, Superpixel Classification, and Shape-Based Models

Ayub *et al.* [26] detected glaucoma via  $k$ -means clustering for color-based segmentation of OD and OC after applying preprocessing and extracting ROI.  $K$  is assigned the value 2 because the entire image is divided into two regions by preprocessing. Arumugam and Nivedha [27] also segmented OD by applying  $k$ -means clustering after preprocessing and removing blood vessels. Cheng *et al.* [2] applied the superpixel classification technique for segmenting OD and OC. The former two methods use a simple linear iterative clustering algorithm to combine neighboring pixels into superpixels. The algorithms applied here are more efficient than the conventional  $k$ -means algorithm as the size of the search region is limited here, which results in less number of distance calculations. In the shape-based techniques, OD is modeled as an elliptical or circular object. These methods try to segment OD by Hough transforms [28] or ellipse fitting [29]. However, these shape-based methods are unsuitable for images of different color intensities and containing blood vessels.

### C. Learning-Based Methods

Many methods such as [30]–[32] used machine learning techniques to segment OD and OC. The work of [30] segmented OD and OC from color fundus images of the retina using a fully automatic regression-based technique. Initially, it applies a circular Hough transform to roughly segment OD. The preliminary shapes of OD and OC are calculated from the approximated OD obtained from the previous step. The method repeatedly learns the final shape of OD and OC from the preliminary shape by a cascaded shape regression technique. For better performance, a data augmentation technique is employed to produce artificial training data. Abràmoff *et al.* [31] used stereo color photographs for the evaluation of automatic OD segmentation. They obtained

a reference segmentation of the neuroretinal rim and OC by glaucoma experts manually. Then, they evaluated stereo pairs and corresponding reference standard by pixel feature classification. However, these approaches rely on the extracted features, which may help them to perform well on specific data sets but not on others. Moreover, manual feature extraction makes these techniques time consuming. In the recent past, many methods have used deep learning for OD and OC segmentation because of its promising results. Lim *et al.* [33] applied a CNN to segment OD and OC. First, they roughly confine the ROI. Then the ROI is transformed into visual features. After that, the method generates a pixel-level probability map of retinal structures through CNN to classify the transformed image. Finally, boundaries of OD and OC are predicted by the segmentation of that map. The work of [3] segmented OD and OC jointly by employing a deep CNN called M-Net. The essential four parts of M-Net are a multiscale input layer, a U-shaped CNN, a side-out layer, and a multilabel loss function. An image pyramid is built by the input layer. The U-shaped CNN is the primary structure that learns the hierarchical features. The side-out layer works as an initial classifier and generates local prediction maps. Lastly, the final segmentation map is created by the multilabel loss function. Additionally, their method applies polar transformation to convert fundus images to a polar coordinate system that produces better-quality segmentation results. Many other methods have also utilized deep learning for the segmentation of OD and OC. Although deep learning-based methods provide excellent results, they take a long time to train the models.

#### D. Fuzzy Logic

The authors of [24] employ fuzzy *c*-means and morphological operations to segment OD and OC but lack in providing exceptional results as compared to state-of-the-art approaches. Some authors, such as [34] and [35], have obtained competent results in regression and classification by using FNNs. Nonetheless, FNNs consume much time in training the parameters of fuzzy rules because FNNs are trained like usual neural networks, which take a lot of time for training. Some researchers have proposed improved algorithms to overcome the problems present in FNNs. The work of [36] proposes a hierarchical hybrid FNN in which a few fuzzy subsystems randomly combine various input features to form an intermediary output, and then a neural network handles these intermediate outputs and the remaining input attributes together to decrease the number of fuzzy rules and input dimension. An online sequential fuzzy extreme learning machine is proposed in [37], where membership functions are assigned the antecedent parameters randomly, and then corresponding subsequent parameters are determined, which reduces the learning time of the algorithm. Sun *et al.* [38] have developed a fuzzy learning system that aggregates the data through *k*-means clustering and derives the membership functions in every fuzzy rule by using an extreme learning machine.

Recently, Feng *et al.* [16] have proposed FBLs, which comprises fuzzy subsystems and enhancement nodes. In this approach, every fuzzy subsystem processes the incoming data, and the features of input data are preserved because the output of

total fuzzy subsystems is dispatched to enhancement nodes to be transformed nonlinearly. Finally, the weights connecting the coefficients of every fuzzy subsystem and output of enhancement nodes with the final output layer are computed through pseudoinverse. The training process in FBLs is significantly reduced because of its flat network. Keeping the need for fast computation and accuracy in mind, we propose a method of OD and OC segmentation, which is less time consuming and provides decent results.

### III. PROPOSED METHOD

Fig. 3 shows an overview of our proposed method of glaucoma detection using OD and OC segmentation. The steps involved are discussed below.

#### A. Extracting the ROI

As shown in Fig. 3, the first step of our segmentation approach is the extraction of an ROI from the original RGB fundus image. We have used the technique of [39] to get the ROI. In addition to the OD area, the ROI also contains some background information to help the network discriminate the OD from the background.

#### B. Data Augmentation

Machine learning and deep learning methods need to be trained on the large data sets for providing optimal performance. However, most of the specialized tasks, such as medical image classifications or segmentation tasks, have insufficient data. Most of the retinal data sets also contain only a few hundred images. The models trained with small data sets do not generalize well and are less accurate in the testing. Research such as [40] demonstrated that data augmentation could prevent this problem. Hence, we have also applied data augmentation in our method to increase the training data size artificially. Our data augmentation consists of flipping left-to-right, flipping top-to-bottom, rotating 90° anticlockwise, and adding noise (consisting of Gaussian noise, and salt and pepper noise). Data augmentation has helped us achieve better results. Fig. 4 shows a sample segmentation without data augmentation, which lacks in providing promising results. Similarly, results without data augmentation are also shown in Fig. 6, 7, 10, and 11.

#### C. Extracting the Red and Green Channel Images

Compared to other channels, the red channel of an RGB fundus image is less influenced by blood vessels and shows more differences between the OD area and background (non-OD area). Hence, it is a suitable choice for OD segmentation. Likewise, the green channel is more appropriate for OC segmentation as the brightness and contrast of OC pixels is very high in this channel. Therefore, we have split the RGB image and fed the red channel and green channel images into two separate FBLs for segmenting OD and OC, respectively. Before inputting the red and green channel images to the FBLs, the mean intensity value is subtracted from the original intensity value of each of

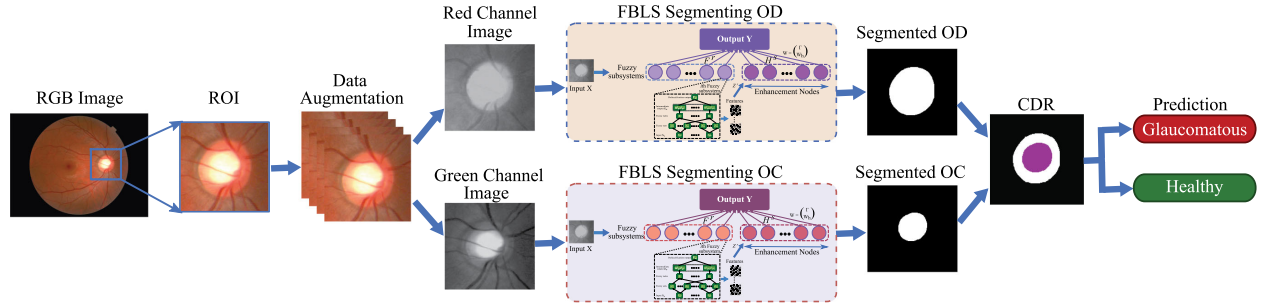


Fig. 3. Overview of our proposed approach of OD and OC segmentation for glaucoma detection using FBLs.

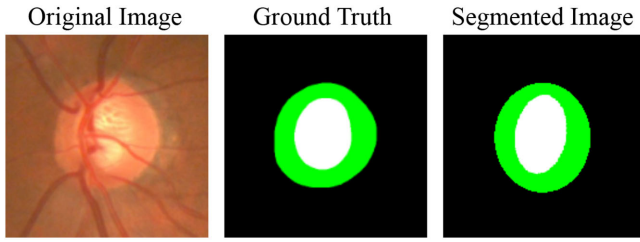


Fig. 4. Sample of segmentation results without applying data augmentation.

the channel images, which exposes the OD and OC areas more clearly for better segmentation.

#### D. OD and OC Segmentation

Here, we input the red/green channel images obtained from the previous step to FBLs and receive the segmented OD/OC as an output. Let  $n$  denotes the quantity of fuzzy subsystems in FBLs and  $m$  represents the enhancement nodes in FBLs. So, the input data are represented as  $X = (x_1, x_2, \dots, x_n)^T \in \mathbb{R}^{n \times m}$ . Initially, the input  $x_q = (x_{q1}, x_{q2}, \dots, x_{qm})$ ,  $q = 1, 2, \dots, n$  is mapped to the  $i$ th fuzzy system by using the first-order Takagi–Sugeno fuzzy model.  $x_{qt}$  denotes a first-order polynomial in the Takagi–Sugeno fuzzy model,  $t = 1, 2, \dots, m$ . It can be calculated as

$$z_{qk}^i = \sum_{t=1}^m \alpha_{kt}^i x_{qt} \quad (1)$$

where  $\alpha_{kt}^i$  is the coefficient and  $k = 1, 2, \dots, K_i$  denotes the fuzzy rule's number in the  $i$ th fuzzy model. We have chosen the Gaussian function as the membership function, which can be defined as shown

$$\mu_{kt}^i(x_{qt}) = e^{-\left(\frac{x_{qt} - c_{kt}^i}{\sigma_{kt}^i}\right)^2} \quad (2)$$

where  $c_{kt}^i$  and  $\sigma_{kt}^i$  represent, respectively, width and center of the Gaussian membership function. We have applied the  $k$ -means technique to get  $K_i$  clustering centers. Because of the  $k$ -means method's randomness in the initial conditions, distinct centers are selected from the input in every fuzzy subsystem that helps extract more features due to the working of all fuzzy subsystems in this ensemble manner. After that, each rule's weighted

activation level can be calculated as

$$\omega_{qk}^i = \frac{\prod_{t=1}^m \mu_{kt}^i(x_{qt})}{\sum_{k=1}^{K_i} \prod_{t=1}^m \mu_{kt}^i(x_{qt})} \quad (3)$$

where  $\prod_{t=1}^m \mu_{kt}^i(x_{qt})$  denotes fire strength of  $i$ th fuzzy subsystem's  $k$ th fuzzy rule. After that, the intermediary output of  $q$ th training sample in the  $i$ th fuzzy subsystem is defined as

$$Z_{qi} = (\omega_{q1}^i z_{q1}^i, \omega_{q2}^i z_{q2}^i, \dots, \omega_{qK_i}^i z_{qK_i}^i). \quad (4)$$

The output vector for the total training samples in an  $i$ th fuzzy subsystem is shown as

$$Z_i = (Z_{1i}, Z_{2i}, \dots, Z_{ni}), i = 1, \dots, r. \quad (5)$$

The intermediate output matrix for  $r$  fuzzy subsystems is shown as

$$Z^r = (Z_1, Z_2, \dots, Z_r) \in \mathbb{R}^{n \times (K_1 + K_2 + \dots + K_r)}. \quad (6)$$

After that, for preserving the characteristics of inputs,  $Z^r$  is nonlinearly transformed by the enhancement nodes, which is represented as

$$H_j = \Psi(Z^r \omega_j + \beta_j), j = 1, \dots, s \quad (7)$$

where  $H_j$  denotes the enhancement nodes transformed from  $Z^r$ ,  $\omega_j$ , and  $\beta_j$  are, respectively, weights and bias terms that connect the fuzzy subsystems' outputs to their correspondent enhancement layers and are selected randomly between values from 0 to 1,  $\Psi(\cdot)$  is Sigmoid activation function. The groups of all the enhancement nodes are computed as

$$H^s = (H_1, H_2, \dots, H_s). \quad (8)$$

The output obtained from each fuzzy subsystem is transmitted to the top layer, along with the output of enhancement nodes. Every fuzzy subsystem will be a multioutput model because the training target  $Y \in \mathbb{R}^{N \times C}$  consists of  $C$  components. The output vector for  $i$ th fuzzy subsystem in  $q$ th training sample is

calculated as

$$\begin{aligned}
 F_{qi} &= \left( \sum_{k=1}^{K_i} \lambda_{k_1}^i \omega_{qk}^i z_{qk}^i, \dots, \sum_{k=1}^{K_i} \lambda_{k_C}^i \omega_{qk}^i z_{qk}^i \right) \\
 &= \left( \sum_{k=1}^{K_i} \lambda_{k_1}^i \omega_{qk}^i \left( \sum_{t=1}^m \alpha_{kt}^i x_{qt} \right) \right), \dots, \\
 &\quad \left( \sum_{k=1}^{K_i} \lambda_{k_C}^i \omega_{qk}^i \left( \sum_{t=1}^m \alpha_{kt}^i x_{qt} \right) \right) \quad (9) \\
 &= \sum_{t=1}^m \alpha_{kt}^i x_{qt} (\omega_{q1}^i, \dots, \omega_{qK_i}^i) \begin{pmatrix} \lambda_{11}^i & \dots & \lambda_{1C}^i \\ \vdots & & \vdots \\ \lambda_{K_i1}^i & \dots & \lambda_{K_iC}^i \end{pmatrix}.
 \end{aligned}$$

The output vector for  $i$ th fuzzy subsystem's total training samples is shown as

$$F_i = (F_{1i}, F_{2i}, \dots, F_{ni}) = D\Omega^i\lambda^i \quad (10)$$

where  $D = \text{diag} \sum_{t=1}^m \alpha_{kt}^i x_{1t}, \dots, \sum_{t=1}^m \alpha_{kt}^i x_{nt}$ , and

$$\Omega^i = \begin{pmatrix} \omega_{11}^i & \dots & \omega_{1K_i}^i \\ \vdots & & \vdots \\ \omega_{n1}^i & \dots & \omega_{nK_i}^i \end{pmatrix}, \lambda^i = \begin{pmatrix} \lambda_{11}^i & \dots & \lambda_{1C}^i \\ \vdots & & \vdots \\ \lambda_{K_i1}^i & \dots & \lambda_{K_iC}^i \end{pmatrix}.$$

The aggregate output of  $r$  fuzzy subsystems is calculated as shown

$$F^r = \sum_{t=1}^r F_i = \sum_{t=1}^r D\Omega^i\lambda^i = D(\Omega^1, \dots, \Omega^r) \begin{pmatrix} \lambda^1 \\ \vdots \\ \lambda^r \end{pmatrix} = D\Omega\Gamma \quad (11)$$

where  $\Omega = (\Omega^1, \dots, \Omega^r)$  is the matrix containing the fire strengths  $\omega_{qk}^i$  and  $\Gamma = ((\lambda^1)^T, \dots, (\lambda^r)^T)^T$  is composed of the parameters to be computed subsequently.

In the end, we connect the output  $F^r$  of all fuzzy subsystems and  $H^s$  of the enhancement nodes to the output of FBLS denoted as  $Y$ , which is defined as

$$\begin{aligned}
 Y &= F^r W_f + H^s W_h \\
 &= D\Omega\Gamma + H^s W_h \\
 &= (D\Omega, H^s) \begin{pmatrix} \Gamma \\ W_h \end{pmatrix} \quad (12) \\
 &= PW
 \end{aligned}$$

where  $W_f$  and  $W_h$ , respectively, are the weights of  $F^r$  and  $H^s$ , and their value is set to 1.  $P = (D\Omega, H^s)$  and  $W$  denote the parameter matrix of fuzzy BLS which is composed of  $\Gamma$  and  $W_h$  and can be calculated through the training targets  $Y : W = P^+ Y$ .

The vector  $P^+$  can be computed by

$$P^+ = \arg \min_W \|PW - Y\|_2^2 + \lambda \|W\|_1. \quad (13)$$

An enhanced least square method is used here to get  $W$  with smaller errors, and  $\lambda$  represents the additional restraints on the summation of squares of weights in [15]. The former part is

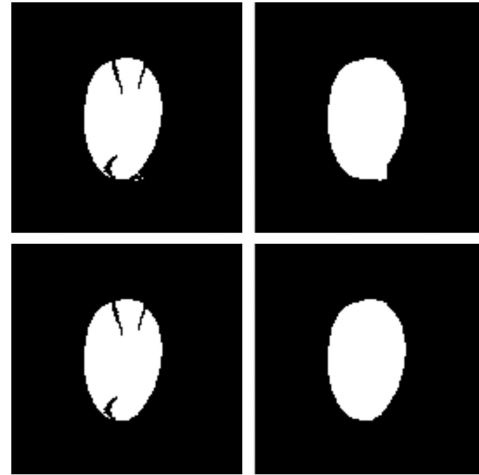


Fig. 5. Top and bottom rows show the segmentation results without and with the area opening operation, respectively.

an  $l_2$ -norm regularization and shows the training errors. The latter part is an  $l_1$ -norm regularization. The use of  $l_1$ -norm regularization makes the proposed model robust against outliers [19] and averts our network from overfitting. The FBLS learns the discriminative features of images and distinguishes OD/OC from the background of retinal images and generates the segmentation maps.

### E. Area Opening and Morphological Closing

In a few images, the segmentation result generated by FBLS contains small pixels outside OD and OC regions, which degrade the segmentation accuracy when the morphological closing operation is performed on these images. Therefore, we first perform the area opening operation on the segmented result obtained from the FBLS to remove those small objects outside the actual OD and OC area and then perform the morphological closing operation. We have used the closing operation to fill the holes in the segmented OD caused by the presence of blood vessels in that region. Fig. 5 shows the closed OD images with and without performing an area opening operation.

## IV. EXPERIMENTAL RESULTS

### A. Data Sets

We have performed experiments on one publicly available data set RIM-ONE-r3 [41] and one data set (SCRID) from the Shanghai Sixth People's Hospital. We could not get the ORIGA data set (used by [3] and [14]) due to the clinical policies of its owner. The RIM-ONE-r3 data set consists of 159 fundus images having a resolution of  $2144 \times 1424$  pixels. The SCRID data set contains 566 images of  $2048 \times 1536$  pixels resolution. We divided the images in training and testing set with a ratio of 80% and 20%, respectively, and applied the data augmentation on only the training images. So, the number of training images became 635 and 2265 for the RIM-ONE-r3 and the SCRID data set, respectively.

**TABLE I**  
TRAINING TIME OF OUR METHOD COMPARED WITH SOME OF THE STATE-OF-THE-ART METHODS (N/A: NOT AVAILABLE)

Method	Training Time (seconds)	Computing Mode
Fu <i>et al.</i> [3]	5241 <sup>¶</sup> / 18759 *	GPU
Sevastopolsky [13]	4623 <sup>¶</sup> / 16247 *	GPU
Maninis <i>et al.</i> [11]	11200 <sup>‡</sup>	N/A
Zilly <i>et al.</i> [12]	3296 <sup>‡</sup>	N/A
Al-Bander <i>et al.</i> [14]	≈ 54000 <sup>†</sup>	GPU
<b>Our Proposed</b>	<b>127.113 <sup>¶</sup> / 231.164 *</b>	<b>GPU</b>

The <sup>†</sup>, <sup>‡</sup>, <sup>¶</sup> symbols represent ORIGA, DRIONS-DB, and RIM-ONE-r3 data sets, respectively. The \* symbol represents the SCRID data set.

## B. Training Time

One of the significant contributions of our method is the efficient training of the network model. Table I shows the training time of our proposed method, along with the training times of the state-of-the-art methods [3], [11]–[14]. We reran the methods of [3] and [13] with the same division of training and testing of 80% and 20%, respectively, and present the consumed time in Table I. The reported times of other methods are taken from the respective papers as we could not get the codes of other methods to run them on our machine. Some methods have not provided their setting information. Hence, we have put “N/A: Not Available” in place of their computing mode. It can be observed that our method outperforms state-of-the-art methods by a significant margin in terms of training time. We ran our method on a workstation having Intel Xeon E5-2630 v4 CPU with NVIDIA Tesla K80 GPU. The training times of our method were 127.113 and 231.164 s for the RIM-ONE-r3 and the SCRID data sets, respectively.

## C. Quantitative Results

We evaluated the segmentation performance of our technique using the Dice coefficient (F1 score), which is used by popular methods such as [42] and [43]. Dice coefficient, represented here as DC, is calculated using

$$DC = \frac{2|A \cap B|}{|A| + |B|} \quad (14)$$

where  $A$  is the predicted segmentation map, and  $B$  is the ground truth segmentation map.

Fig. 6 and 7 show the comparison of OD and OC segmentation results of our method with other works in the literature. The comparison consists of the DC scores. As discussed earlier, we reran the codes of [3] and [13]. The data for other methods are taken from [13], [14], and [32]. The DC score of our method for OD segmentation for the RIM-ONE-r3 data set is 0.973. In addition to this, our proposed method achieves good results on OC segmentation as we have employed an entire FBLN-based neural network to segment OC. As shown in Fig. 6, the DC score of our approach for OC segmentation for the RIM-ONE-r3 data set is 0.882. Some methods have not reported the DC scores for OC segmentation in their papers; that is why DC scores for OC segmentation are not shown at some places in Fig. 6. The DC scores of our method for OD and OC segmentation

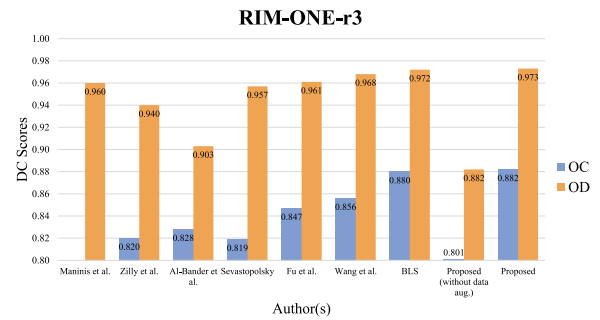


Fig. 6. DC scores of our method, [11], [13], [3], [12], [14], and [32] for OD and OC segmentation on the RIM-ONE-r3.

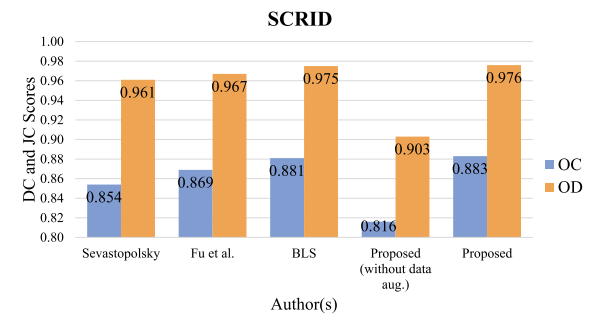


Fig. 7. DC scores of our method, [13], and [3] for OD and OC segmentation on the SCRID data set.

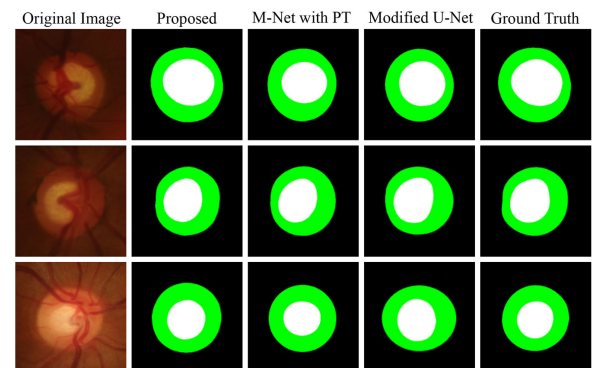


Fig. 8. Segmentation results of our method compared with [3] and [13], and the ground truth images of the RIM-ONE-r3 data set.

for the SCRID data set are 0.976 and 0.883, respectively, as presented in Fig. 7. It is evident from these results that our method outperforms state-of-the-art methods in OD and OC segmentation.

## D. Qualitative Results

Fig. 8 and 9 show the segmentation results of our method in comparison to [3] and [13] on RIM-ONE-r3 and SCRID data sets, respectively. The first column contains the original ROI images; the second column shows the images segmented by our method, the third column shows the result of Fu *et al.* [3], the fourth column contains the segmentation result of [13], and the fifth column shows the ground truth images. These results

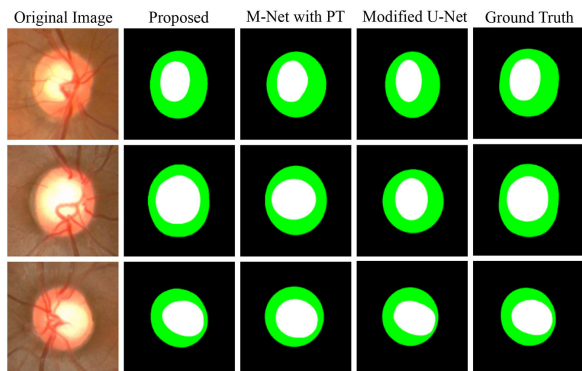


Fig. 9. Segmentation results of our method compared with [3] and [13], and the ground truth images of the SCRID data set.

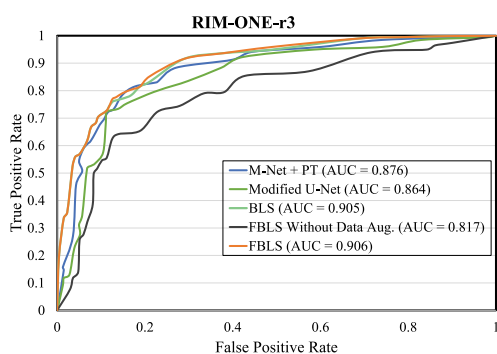


Fig. 10. ROC curves with AUC scores for glaucoma diagnosis on the RIM-ONE-r3 data set.

exhibit that our method provides better results of OD and OC segmentation when compared to the other two techniques.

### E. Glaucoma Screening

We also performed a binary classification on images as being healthy or glaucoma affected with the help of computed CDRs because CDR is an important clinical indicator of glaucoma progression.  $CDR = VD_{cup}/VD_{disk}$  where,  $VD_{cup}$  and  $VD_{disk}$  respectively, represent the vertical diameters of OC and OD. Due to better segmentation of OC, we calculate the CDR more accurately, and therefore, achieve better results of glaucoma screening. We compared our classification results with the experts' evaluation results provided with the data sets and computed the accuracy of our method. Fig. 10 and 11 show the glaucoma diagnosis performance of our method by reporting the receiver operating characteristic (ROC) curve with AUC scores for the RIM-ONE-r3 and the SCRID data sets, respectively. Our method achieves the best AUC scores of 0.906 and 0.923 for glaucoma screening on the RIM-ONE-r3 and the SCRID data sets, respectively.

We also present the classification errors (calculated as incorrect predictions / total predictions) in the Table II. It is obvious that our method has lesser errors, 0.093 and 0.061 for the RIM-ONE-r3 and the SCRID data sets, respectively, than the other methods and, hence, outperforms them here as well.

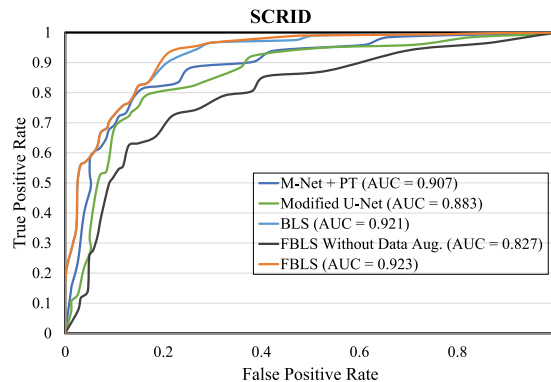


Fig. 11. ROC curves with AUC scores for glaucoma diagnosis on the SCRID data set.

TABLE II  
CLASSIFICATION ERRORS ON RIM-ONE-R3 AND SCRID

Dataset	M-Net+PT	Modified U-Net	BLS	Proposed
RIM-ONE-r3	0.156	0.218	0.125	<b>0.093</b>
SCRID	0.088	0.123	0.079	<b>0.061</b>

### F. Significance Test

To show the statistical significance in the calculated CDRs, we have conducted a nonparametric statistical test, called the Friedman test [44] with  $\alpha = 0.05$ , on the CDRs calculated by M-Net+PT [3], modified U-Net [13], and our proposed method FBLs. We applied the Friedman test on the test set images, which are 20% of each data set. Hence, the number of values becomes 32 from the RIM-ONE-r3 and 113 from the SCRID data set. Our method FBLs achieved significantly better results by reporting  $p = 0.009$  on the RIM-ONE-r3 data set.

However, the Friedman test only tells that CDRs are statistically different, but it does not tell which group is exactly different. Hence, to see where the difference exists, we need to perform a post hoc test. We performed a post hoc test by running the Wilcoxon signed-rank test [45]. The Wilcoxon signed-rank test is a nonparametric test that finds the difference between two groups of data. So, we performed this test on different combinations of CDRs computed by these three methods as: 1) FBLs to M-Net+PT; 2) FBLs to modified U-Net; 3) M-Net+PT to modified U-Net, to find which one of them is significantly different. Nevertheless, before looking at the results of Wilcoxon signed-rank, we need to consider one more thing. As we are performing multiple tests for comparison, some of these tests will give a  $p$ -value less than 0.05 by chance [46]. To overcome this, we need to apply a Bonferroni adjustment to the results obtained from the Wilcoxon tests. The Bonferroni adjustment is computed by dividing the initial significance level (0.05) by the number of tests performed. In our case, the new significance level is obtained as  $0.05/3 = 0.017$  because we are performing three comparison tests. When our method is compared with M-Net+PT, the Wilcoxon signed-rank test gave  $p = 0.006$ , which is less than 0.017. Similarly,  $p = 0.003$  is obtained when we compare our method with modified U-Net. The comparison results of M-Net+PT and modified U-Net were not statistically significant

**TABLE III**  
DC AND AUC SCORES OF CROSS-TRAINING

Technique	DC Score for OD Segmentation	DC Score for OC Segmentation	AUC
Sevastopolsky [13]	0.939	0.813	0.845
Fu <i>et al.</i> [3]	0.948	0.838	<b>0.864</b>
Wang <i>et al.</i> [32]	<b>0.959</b>	0.847	0.853
BLS	0.951	0.849	0.856
Proposed	0.953	<b>0.856</b>	0.860

because  $p = 0.66$  was achieved when these two methods were compared.

In the same manner, we performed the Friedman test on the SCRID data set. Here, also, our method obtained statistically significant results by reporting  $p = 0.001$ . Besides, we also conducted a post hoc test with the Wilcoxon signed-rank test with a Bonferroni adjustment applied. There was no significant difference between M-Net+PT and modified U-Net  $p = 0.761$ . Nevertheless, there was significant difference in the results of FBLS to M-Net+PT  $p = 0.002$  and FBLS to modified U-Net  $p = 0.003$ .

### G. Using SCRID for Training and RIM-ONE-r3 for Testing

To further testify the robustness of our technique, we also experimented the cross-training by using the SCRID data set for training and the RIM-ONE-r3 data set for testing. The obtained results are shown in Table III. In these cross-training results, our approach has gotten the best DC score of 0.856 for OC segmentation, along with the second-best DC score for OD segmentation and the second-best AUC score of 0.953 and 0.860, respectively. By looking at these results, we can claim that our method provides competent results on unseen images when compared with the other state-of-the-art methods.

### H. Results on the REFUGE and the DRISHTI-GS1 Data Sets

We also performed the experiments on the REFUGE [42] and DRISHTI-GS1 [43] data sets to show the strength and potential of our method. The REFUGE data set consists of 1200 images equally divided into three parts: training set, validation set, and test set (each of the three parts contains 400 images). The resolution of training set images is  $2124 \times 2056$  pixels, and the validation and test images are of the  $1634 \times 1634$  pixels size. We trained our technique on the training set and evaluated it on the test set images. Then, we compared our results with the results of the top three teams from the REFUGE challenge [42] organized in conjunction with MICCAI 2018. The DC scores compared with the best three methods in terms of OD and OC segmentation are reported in Table IV. Our method obtained the best DC scores of 0.9743 and 0.8845 for OD and OC segmentation, respectively.

We also compared the AUC scores of our method with the top three methods in terms of the best AUC scores. Those results are presented in Table V. Here, our approach obtained the third-best AUC score of 0.9721. These results also demonstrate a

**TABLE IV**  
COMPARISON OF DC SCORES ON THE REFUGE

Technique	For OD Segmentation	For OC Segmentation
Team CUHKMED	0.9602	0.8826
Team Masker	0.9464	0.8837
Team BUCT	0.9525	0.8728
BLS	0.9621	0.8823
Proposed	<b>0.9743</b>	<b>0.8845</b>

**TABLE V**  
AUC SCORES ON THE REFUGE DATA SET

Technique	AUC Score
Team VRT	<b>0.9885</b>
Team SDSAIRC	0.9817
Team CUHKMED	0.9644
BLS	0.9673
Proposed	0.9721

**TABLE VI**  
COMPARISON OF OUR METHOD'S DC AND AUC SCORES WITH STATE-OF-THE-ART METHODS ON THE DRISHTI-GS1 DATA SET

Technique	DC Score for OD Segmentation	DC Score for OC Segmentation	AUC
Sevastopolsky [13]	0.947	0.850	0.849
Fu <i>et al.</i> [3]	0.953	0.861	0.864
Wang <i>et al.</i> [32]	0.965	0.858	0.858
BLS	0.964	0.865	0.870
Proposed	<b>0.968</b>	<b>0.880</b>	<b>0.887</b>

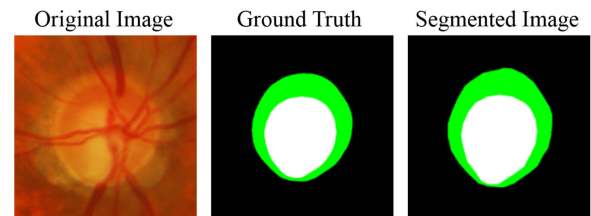


Fig. 12. Sample of the performance on a noisy image.

satisfactory performance of our method on the REFUGE data set when compared with state-of-the-art algorithms.

The DRISHTI-GS1 data set comprises 101 images having a resolution of  $2896 \times 1944$  pixels. The data set is split into training and test set containing 50 and 51 images, respectively. The DC scores for OD and OC segmentation and AUC score of our approach compared with [3], [13], and [32] are shown in Table VI. As seen from the results in Table VI, our method has achieved the best DC scores of 0.968 and 0.880 for segmenting OD and OC, respectively. Moreover, our technique has also gotten the best AUC score of 0.887. These results also show that our method performs better than some of the best algorithms on the DRISHTI-GS1 data set.

### I. Segmentation in Noisy Images

The presence of noise in the retinal images makes it hard to perform an accurate segmentation of OD/OC. We tested the performance of our technique on noisy images, and one sample segmentation is shown in Fig. 12. These results also indicate that our approach generates decent results on noisy images.

## J. Limitation

One of the limitations of our method is that it requires preprocessing and postprocessing for providing optimal results. Another limitation may be the need to extract individual channels to perform the segmentation (red channel for OD and green channel for OC segmentation), which is unlike some of the other methods which directly work on RGB fundus images.

## V. CONCLUSION

In this article, we had presented a novel technique of OD and OC segmentation, which adopted the FBLs. The proposed approach outperformed the state-of-the-art techniques in terms of network training time, OD and OC segmentation, and glaucoma screening results. The main advantage of our method was the efficient training process due to which it can be trained even on machines without having a GPU. Because of the fast training, our proposed work used an entire FBLs-based neural network for OC segmentation, which helped it attain more accurate OC segmentation results. The experiments performed on the RIM-ONE-r3 and the SCRID data sets showed promising results of OD and OC segmentation. Additionally, CDR was calculated with the help of the segmented OD and OC. With the help of the calculated CDR, our method provided better performance on glaucoma diagnosis as compared to many contemporary glaucoma screening algorithms.

## REFERENCES

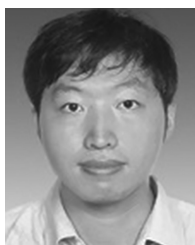
- [1] GRF, *Glaucoma Facts and Stats*. (2019). [Online]. Available: <https://www.glaucoma.org/glaucoma/glaucoma-facts-and-stats.php>
- [2] J. Cheng et al., "Superpixel classification based optic disc and optic cup segmentation for glaucoma screening," *IEEE Trans. Med. Imag.*, vol. 32, no. 6, pp. 1019–1032, Jun. 2013.
- [3] H. Fu, J. Cheng, Y. Xu, D. W. K. Wong, J. Liu, and X. Cao, "Joint optic disc and cup segmentation based on multi-label deep network and polar transformation," *IEEE Trans. Med. Imag.*, vol. 37, no. 7, pp. 1597–1605, Jul. 2018.
- [4] H. A. Nugroho, W. K. Z. Oktoeberza, A. Erasari, A. Utami, and C. Cahyono, "Segmentation of optic disc and optic cup in colour fundus images based on morphological reconstruction," in *Proc. Int. Conf. Inf. Technol. Elect. Eng.*, 2017, pp. 1–5.
- [5] A. Almazroa, R. Burman, K. Raahemifar, and V. Lakshminarayanan, "Optic disc and optic cup segmentation methodologies for glaucoma image detection: A survey," *J. Ophthalmol.*, vol. 2015, pp. 180 972:1–180 972:28, 2015.
- [6] S. Aleem, B. Sheng, P. Li, P. Yang, and D. D. Feng, "Fast and accurate retinal identification system: Using retinal blood vasculature landmarks," *IEEE Trans. Ind. Informat.*, vol. 15, no. 7, pp. 4099–4110, Jul. 2019.
- [7] S. Omid, J. Shanbehzadeh, Z. Ghassabi, and S. S. Ostadzadeh, "Optic disc detection in high-resolution retinal fundus images by region growing," in *Proc. Int. Conf. Biomed. Eng. Informat.*, 2015, pp. 101–105.
- [8] S. Shao, S. McAleer, R. Yan, and P. Baldi, "Highly accurate machine fault diagnosis using deep transfer learning," *IEEE Trans. Ind. Informat.*, vol. 15, no. 4, pp. 2446–2455, Apr. 2019.
- [9] C. Sun, M. Ma, Z. Zhao, S. Tian, R. Yan, and X. Chen, "Deep transfer learning based on sparse autoencoder for remaining useful life prediction of tool in manufacturing," *IEEE Trans. Ind. Informat.*, vol. 15, no. 4, pp. 2416–2425, Apr. 2019.
- [10] X. Yuan, B. Huang, Y. Wang, C. Yang, and W. Gui, "Deep learning-based feature representation and its application for soft sensor modeling with variable-wise weighted SAE," *IEEE Trans. Ind. Informat.*, vol. 14, no. 7, pp. 3235–3243, Jul. 2018.
- [11] K.-K. Maninis, J. Pont-Tuset, P. Arbeláez, and L. Van Gool, "Deep retinal image understanding," in *Proc. Int. Conf. Med. Image Comput. Comput.-Assisted Intervention*, 2016, pp. 140–148.
- [12] J. Zilly, J. M. Buhmann, and D. Mahapatra, "Glaucoma detection using entropy sampling and ensemble learning for automatic optic cup and disc segmentation," *Computerized Med. Imag. Graph.*, vol. 55, pp. 28–41, 2017.
- [13] A. Sevastopolsky, "Optic disc and cup segmentation methods for glaucoma detection with modification of U-Net convolutional neural network," *Pattern Recognit. Image Anal.*, vol. 27, no. 3, pp. 618–624, 2017.
- [14] B. Al-Bander, B. M. Williams, W. Al-Nuaimy, M. A. Al-Tae, H. Pratt, and Y. Zheng, "Dense fully convolutional segmentation of the optic disc and cup in colour fundus for glaucoma diagnosis," *Symmetry*, vol. 10, no. 4, pp. 87:1–87:16, 2018.
- [15] C. L. P. Chen and Z. Liu, "Broad learning system: An effective and efficient incremental learning system without the need for deep architecture," *IEEE Trans. Neural Netw. Learn. Syst.*, vol. 29, no. 1, pp. 10–24, Jan. 2018.
- [16] S. Feng and C. L. P. Chen, "Fuzzy broad learning system: A novel neuro-fuzzy model for regression and classification," *IEEE Trans. Cybern.*, vol. 50, no. 2, pp. 414–424, Feb. 2020.
- [17] J. Jin, Z. Liu, and C. L. P. Chen, "Discriminative graph regularized broad learning system for image recognition," *Sci. China Inf. Sci.*, vol. 61, no. 11, pp. 112 209:1–112 209:14, 2018.
- [18] C. L. P. Chen, Z. Liu, and S. Feng, "Universal approximation capability of broad learning system and its structural variations," *IEEE Trans. Neural Netw. Learn. Syst.*, vol. 30, no. 4, pp. 1191–1204, Apr. 2019.
- [19] J.-W. Jin and C. L. P. Chen, "Regularized robust broad learning system for uncertain data modeling," *Neurocomputing*, vol. 322, pp. 58–69, 2018.
- [20] N. Upasani and H. Om, "Evolving fuzzy min-max neural network for outlier detection," *Procedia Comput. Sci.*, vol. 45, pp. 753–761, 2015.
- [21] G.-D. Wu and P.-H. Huang, "A vectorization-optimization-method-based type-2 fuzzy neural network for noisy data classification," *IEEE Trans. Fuzzy Syst.*, vol. 21, no. 1, pp. 1–15, Feb. 2013.
- [22] S.-B. Roh, S.-K. Oh, and W. Pedrycz, "Identification of black plastics based on fuzzy RBF neural networks: Focused on data preprocessing techniques through fourier transform infrared radiation," *IEEE Trans. Ind. Informat.*, vol. 14, no. 5, pp. 1802–1813, May 2018.
- [23] A. Septiarni, A. Harjoko, R. Pulungan, and R. Ekantini, "Optic disc and cup segmentation by automatic thresholding with morphological operation for glaucoma evaluation," *Signal, Image Video Process.*, vol. 11, no. 5, pp. 945–952, 2017.
- [24] N. E. A. Khalid, N. M. Noor, and N. M. Ariff, "Fuzzy c-Means (FCM) for optic cup and disc segmentation with morphological operation," *Procedia Comput. Sci.*, vol. 42, pp. 255–262, 2014.
- [25] M. Abdullah, M. M. Fraz, and S. A. Barman, "Localization and segmentation of optic disc in retinal images using circular hough transform and grow-cut algorithm," *PeerJ*, vol. 4, pp. e2003:1–e2003:22, 2016.
- [26] J. Ayub et al., "Glaucoma detection through optic disc and cup segmentation using k-mean clustering," in *Proc. Int. Conf. Comput., Electron. Elect. Eng.*, 2016, pp. 143–147.
- [27] G. Arumugam and S. Nivedha, "Optic disc segmentation based on independent component analysis and k-means clustering," *Int. J. Emerg. Trends Technol. Comput. Sci.*, vol. 2, no. 6, pp. 246–251, 2013.
- [28] J. Sigut, O. Nunez, F. Fumero, M. Gonzalez, and R. Arnav, "Contrast based circular approximation for accurate and robust optic disc segmentation in retinal images," *PeerJ*, vol. 5, pp. e3763:1–e3763:18, 2017.
- [29] P. M. D. S. Pallawala, W. Hsu, M. L. Lee, and K.-G. A. Eong, "Automated optic disc localization and contour detection using ellipse fitting and wavelet transform," in *Proc. Eur. Conf. Comput. Vision*, 2004, pp. 139–151.
- [30] S. Sedai, P. K. Roy, D. Mahapatra, and R. Garnavi, "Segmentation of optic disc and optic cup in retinal fundus images using shape regression," in *Proc. Annu. Int. Conf. IEEE Eng. Med. Biol. Soc.*, 2016, pp. 3260–3264.
- [31] M. D. Abrámovič et al., "Automated Segmentation of the optic disc from stereo color photographs using physiologically plausible features," *Investigative Ophthalmology Visual Sci.*, vol. 48, no. 4, pp. 1665–1673, 2007.
- [32] S. Wang, L. Yu, X. Yang, C.-W. Fu, and P.-A. Heng, "Patch-based output space adversarial learning for joint optic disc and cup segmentation," *IEEE Trans. Med. Imag.*, vol. 38, no. 11, pp. 2485–2495, Nov. 2019.
- [33] G. Lim, Y. Cheng, W. Hsu, and M. L. Lee, "Integrated optic disc and cup segmentation with deep learning," in *Proc. IEEE Int. Conf. Tools Artif. Intell.*, 2015, pp. 162–169.
- [34] V. Sumati, C. Patvardhan, S. Paul, L. Singh, and V. M. Swarup, "Application of interval type-2 submethod neural fuzzy inference system in control and function approximation," in *Proc. IEEE Int. Conf. Fuzzy Syst.*, 2017, pp. 1–6.
- [35] S. Feng and C. L. P. Chen, "A fuzzy restricted Boltzmann machine: Novel learning algorithms based on the crisp possibilistic mean value of fuzzy numbers," *IEEE Trans. Fuzzy Syst.*, vol. 26, no. 1, pp. 117–130, Feb. 2018.

- [36] D. Wang, X.-J. Zeng, and J. A. Keane, "Hierarchical hybrid fuzzy-neural networks for approximation with mixed input variables," *Neurocomputing*, vol. 70, pp. 3019–3033, 2007.
- [37] H.-J. Rong, G.-B. Huang, N. Sundararajan, and P. Saratchandran, "Online sequential fuzzy extreme learning machine for function approximation and classification problems," *IEEE Trans. Syst., Man, Cybern., Part B (Cybern.)*, vol. 39, no. 4, pp. 1067–1072, Aug. 2009.
- [38] Z.-L. Sun, K.-F. Au, and T.-M. Choi, "A neuro-fuzzy inference system through integration of fuzzy logic and extreme learning machines," *IEEE Trans. Syst., Man, Cybern., Part B (Cybern.)*, vol. 37, no. 5, pp. 1321–1331, Oct. 2007.
- [39] H. Yu *et al.*, "Fast localization and segmentation of optic disk in retinal images using directional matched filtering and level sets," *IEEE Trans. Inf. Technol. Biomed.*, vol. 16, no. 4, pp. 644–657, Jul. 2012.
- [40] T. Huynh-The, C.-H. Hua, and D.-S. Kim, "Encoding pose features to images with data augmentation for 3D action recognition," *IEEE Trans. Ind. Informat.*, vol. 16, no. 5, pp. 3100–3111, May 2020.
- [41] F. Fumero, S. Alayon, J. L. Sanchez, J. Sigut, and M. Gonzalez-Hernandez, "RIM-ONE: An open retinal image database for optic nerve evaluation," in *Proc. Int. Symp. Comput.-Based Med. Syst.*, 2011, pp. 1–6.
- [42] J. I. Orlando *et al.*, "REFUGE challenge: A unified framework for evaluating automated methods for glaucoma assessment from fundus photographs," *Med. Image Anal.*, vol. 59, 2020, Art. no. 101570.
- [43] J. Sivaswamy, A. Chakravarty, G. D. Joshi, and T. A. Syed, "A comprehensive retinal image dataset for the assessment of glaucoma from the optic nerve head analysis," *JSM Biomed. Imag. Data Papers*, vol. 2, no. 1, 2015, Art. no. 1004.
- [44] M. Friedman, "The use of ranks to avoid the assumption of normality implicit in the analysis of variance," *J. Amer. Statist. Assoc.*, vol. 32, no. 200, pp. 675–701, 1937.
- [45] F. Wilcoxon, "Individual comparisons by ranking methods," *Biometrics Bulletin*, vol. 1, no. 6, pp. 80–83, 1945.
- [46] J. H. McDonald, *Handbook of Biological Statistics*, 3rd ed. Baltimore, MD, USA: Sparky House Publishing, 2014.



**Riaz Ali** received the B.Eng. degree in software engineering from the Mehran University of Engineering & Technology, Jamshoro, Pakistan, in 2010, and is currently pursuing the M.Eng. degree in computer science with the Department of Computer Science and Engineering, Shanghai Jiao Tong University, Shanghai, China.

His current research interests include medical image analysis, broad learning system, and computer vision.



**Bin Sheng** received the B.A. degree in English and the B.Eng. degree in computer science from the Huazhong University of Science and Technology, Wuhan, China, in 2004, and the M.Sc. degree in software engineering from the University of Macau, Taipa, Macau, in 2007, and the Ph.D. degree in computer science and engineering from The Chinese University of Hong Kong, Shatin, Hong Kong, in 2011.

He is currently an Associate Professor with the Department of Computer Science and Engineering, Shanghai Jiao Tong University, Shanghai, China.

His current research interests include virtual reality and computer graphics.

Dr. Sheng is an Associate Editor of the IEEE TRANSACTIONS ON CIRCUITS AND SYSTEMS FOR VIDEO TECHNOLOGY.



**Ping Li** (Member, IEEE) received the Ph.D. degree in computer science and engineering from The Chinese University of Hong Kong, Shatin, Hong Kong, in 2013.

He is currently a Research Assistant Professor with The Hong Kong Polytechnic University, Kowloon, Hong Kong. He has one image/video processing national invention patent, and has excellent research project reported worldwide by *ACM TechNews*. His current research interests include artistic rendering and synthesis, and creative media.



**Yan Chen** received the M.D. degree in ophthalmology from the Fudan University, Shanghai, China, in 2010.

She is currently an Attending Doctor with the Department of Ophthalmology, Shanghai Jiao Tong University Affiliated Sixth People's Hospital, Shanghai, China. Her current research interests include glaucoma, cataract, and biological image processing.



**Huating Li** received the Ph.D. degree in internal medicine from Shanghai Jiao Tong University, Shanghai, China, and Pennington Biomedical Research Center, Baton Rouge, LA, USA, in 2011.

She is currently an Associate Professor with the Shanghai Jiao Tong University Affiliated Sixth People's Hospital and the Shanghai Diabetes Institute. Her current research interests include the role of cytokines in the development of fatty liver disease, diabetes, and other obesity-related diseases.

related diseases.

Dr. Li was the recipient of the Shanghai Science and Technology Progress Award.



**Po Yang** received the B.Sc. degree in computer science from Wuhan University, Wuhan, China, in 2004, the M.Sc. degree in computer science from the University of Bristol, Bristol, U.K., in 2006, and the Ph.D. degree in electronic engineering from Staffordshire University, Stoke-on-Trent, U.K., in 2011.

He is currently a Senior Lecturer in Large Scale Data Fusion with the Department of Computer Science, The University of Sheffield, Sheffield, U.K. He holds a strong tracking of

high-quality publications and research experiences. He has authored or co-authored over 40 papers. His current research interests include Internet of Things, RFID and indoor localization, pervasive health, image processing, GPU, and parallel computing.



**Younhyun Jung** received the B.Sc. degree in computer science from Inha University, Incheon, Korea, in 2008, and the Ph.D. degree in computer science from The University of Sydney, NSW, Sydney, Australia, in 2016.

He is currently a Postdoctoral Research Fellow in computer science with The University of Sydney. He was a Software Engineer with Samsung Electronics from 2007 to 2010. His current research interests include volume rendering and multimodal medical image visualization.



**Jinman Kim** received the B.S. (Hons.) and Ph.D. degrees in computer science from The University of Sydney, Sydney, NSW, Australia, in 2001 and 2006, respectively.

Since 2006, he has been a Research Associate with the leading teaching hospital, the Royal Prince Alfred, Camperdown, NSW, Australia. From 2008 to 2012, he was an ARC Postdoctoral Research Fellow, one year leave from 2009 to 2010 to join the MIRALab Research Group, Geneva, Switzerland, as a Marie Curie

Senior Research Fellow. Since 2013, he has been with the School of Information Technologies, The University of Sydney, where he was a Senior Lecturer, and became an Associate Professor in 2016. His current research interests include medical image analysis and visualization, computer aided diagnosis, and telehealth technologies.



**C. L. Philip Chen** (Fellow, IEEE) received the M.S. degree in electrical engineering from the University of Michigan, Ann Arbor, MI, USA, in 1985, and the Ph.D. degree in electrical engineering from Purdue University, West Lafayette, IN, USA, in 1988.

He is currently a Chair Professor and the Dean of the School of Computer Science and Engineering, South China University of Technology, Guangzhou, China. Being a Program Evaluator of the Accreditation Board of Engineering and Technology Education (ABET) in the USA, for computer engineering, electrical engineering, and software engineering programs, he successfully architects the University of Macau's Engineering and Computer Science programs receiving accreditations from Washington/Seoul Accord through Hong Kong Institute of Engineers (HKIE), of which is considered as his utmost contribution in engineering/computer science education for Macau as the former Dean of the Faculty of Science and Technology. His current research interests include systems, cybernetics, and computational intelligence.

Prof. Chen is a Fellow of AAAS, IAPR, CAA, and HKIE; a Member of Academia Europaea (AE), European Academy of Sciences and Arts (EASA), and International Academy of Systems and Cybernetics Science (IASCYS). He was the recipient of the IEEE Norbert Wiener Award in 2018 for his contribution in systems and cybernetics, and machine learning. He is also a 2018 highly cited researcher in Computer Science by Clarivate Analytics in a 2018. He was the recipient of the 2016 Outstanding Electrical and Computer Engineers Award from his alma mater, Purdue University, after he graduated from the University of Michigan at Ann Arbor, Ann Arbor, MI, USA in 1985. He was the President of the IEEE Systems, Man, and Cybernetics Society from 2012 to 2013, and the Editor-in-Chief of the IEEE TRANSACTIONS ON SYSTEMS, MAN, AND CYBERNETICS: SYSTEMS. Currently, he is the Editor-in-Chief of the IEEE TRANSACTIONS ON CYBERNETICS, and an Associate Editor of the IEEE TRANSACTIONS ON FUZZY SYSTEMS. And currently, he is a Vice President of Chinese Association of Automation (CAA).